Spectrochimica Acta Part A: Molecular and Biomolecular Spectroscopy 307 (2024) 123672

Contents lists available at ScienceDirect

Spectrochimica Acta Part A:
Molecular and Biomolecular Spectroscopy

journal homepage: www.journals.elsevier.com/spectrochimica-acta-part-a-molecular-and-biomolecular-spectroscopy

Asbestos detection in construction and demolition waste by different classification methods applied to short-wave infrared hyperspectral images

G. Bonifazi [a], G. Capobianco [a,*], S. Serranti [a], O. Trotta [a], S. Bellagamba [b], S. Malinconico [b], F. Paglietti [b]

[a] Department of Chemical Engineering Materials & Environment, Sapienza University of Rome, Rome, Italy
[b] Italian Workers Compensation Authority (INAIL), Department of Technological Innovations and Safety of Plants, Products and Anthropic Settlements, Rome, Italy

HIGHLIGHTS

- Characterization of Asbestos Containing Materials (ACMs) by SWIR-HSI.
- Automated non-destructive ACMs detection in Construction and Demolition Waste (C&DW).
- Evaluation of different HSI classification models and comparison with micro-XRF maps.
- Proposing a robust and efficient strategy for classifying hazardous materials in C&DW.

GRAPHICAL ABSTRACT

ARTICLE INFO

Keywords:
Asbestos
Construction and demolition waste
Hyperspectral imaging
Micro-XRF
Hi-PLSDA
ECOC-SVM
PCA-kNN

ABSTRACT

In this study, different multivariate classification methods were applied to hyperspectral images acquired, in the short-wave infrared range (SWIR: 1000–2500 nm), to define and evaluate quality control actions applied to construction and demolition waste (C&DW) flow streams, with particular reference to the detection of hazardous material as asbestos. Three asbestos fibers classes (i.e., amosite, chrysotile and crocidolite) inside asbestos-containing materials (ACM) were investigated. Samples were divided into two groups: calibration and validation datasets. The acquired hyperspectral images were first explored by Principal Component Analysis (PCA). The following multivariate classification methods were selected in order to verify and compare their efficiency and robustness: Hierarchical Partial Least Squares-Discriminant Analysis (Hi-PLSDA), Principal Component Analysis k-Nearest Neighbors (PCA-kNN) and Error Correcting Output Coding with Support Vector Machines (ECOC-SVM). The classification results obtained for the three models were evaluated by prediction maps and the values of performance parameters (*Sensitivity* and *Specificity*). Micro-X-ray fluorescence (micro-XRF) maps confirmed the correctness of classification results. The results demonstrate how SWIR-HSI technology, coupled with multivariate analysis modelling, is a promising approach to develop both “off-line” and “online” fast, reliable and robust quality control strategies, finalized to perform a quick assessment of ACM presence.

* Corresponding author.
E-mail address: giuseppe.capobianco@uniroma1.it (G. Capobianco).

https://doi.org/10.1016/j.saa.2023.123672
Received 23 May 2023; Received in revised form 17 November 2023; Accepted 19 November 2023
Available online 20 November 2023

1. Introduction

Every year a huge amount of construction and demolition waste (C&DW) is generated, arising from construction sites and the demolition of buildings and infrastructures. These materials have a high potential for recycling and reuse [1], in particular, inert C&DW (i.e., concrete and brick) can be recycled into aggregates (RA) [2,3]. However, a small portion of C&DW contains asbestos, a hazardous material that severely impacts human health, natural environment and society [4]. Asbestos is the common name for a family of fibrous minerals such as chrysotile and crocidolite, the most common asbestos minerals on earth, followed by amosite [5,6]. Asbestos was utilized in an endless number of industrial applications due to its technological properties and outstanding characteristics, such as resistance to heat and chemicals and its relatively low cost [6,7]. Asbestos is commonly found in the so-called asbestos-containing materials (ACM), in which asbestos fibers are combined with cement matrices, and nowadays, there are still more than 2 billion m^2 of cement-asbestos slates and approximately 300 million m^3 of friable asbestos in both indoor and outdoor environments [5]. However, despite its properties, since the '80s, asbestos has been recognized as hazardous to human health and banned in many industrialized countries. Asbestos is potentially dangerous due to the potential release in the air of fibers, whose harmfulness is well known if inhaled or ingested due to degradation/alteration phenomena and manipulation/handling activities [8,9].

During the C&DW recycling process, ACM must be collected and separated from the other wastes to minimize contamination risks. The regulations required ACM to be removed through packaging and storage in controlled landfills, so they were no longer hazardous. Moreover, the subsequent detection of ACM in C&DW makes recycling impractical, and thus it is dumped in landfills [10]. Environmental impacts associated with low C&DW recycling rates include high energy consumption and depletion of valuable resources in the production of building materials, both for new construction and post-disaster reconstruction, rather than using existing waste materials [11–13]. So, a solution capable of separating hazardous from non-hazardous materials is fundamental and needed to reduce landfilling and improve C&DW recycling.

Recently an alternative way to dumping ACM was shown by several authors [14,15], based on an industrial process for the thermal transformation of ACM and recycling of the end product. This process allows the direct annealing of cement-asbestos slates or loose friable packages using a tunnel kiln with certain temperature conditions. The composition results are similar to a natural clinker except for a more significant aluminium, iron and magnesium content. It can eventually be recycled as a secondary raw material for producing various industrial materials [15]. From this perspective, identifying and removing ACM from C&DW could be profitable to manage ACM and recycle C&DW. In order to find the best solution to characterize and separate this waste, it is necessary to adopt innovative technology that can identify hazardous contaminants such as asbestos fibers in a C&DW stream.

Hyperspectral imaging (HSI) could be a valuable solution to detect asbestos fibers and to identify different types of ACM and C&DW. Indeed, different studies have been carried out to characterize asbestos fibers in ACM and to classify ACM samples from C&DW, using HSI techniques [16–20]. HSI has the advantage of being non-destructive, non-invasive and it does not need any sample preparation, thus allowing the acquisition of large quantities of samples in a short time and to handle huge amounts of C&DW, improving worker safety at the same time.

The proposed work aimed to apply HSI working in the Short-Wave InfraRed range (SWIR: from 1000 to 2500 nm) for classifying and identifying different kinds of C&DW and ACM samples. The novelty of this work is the comparison of different classification techniques to determine the best approach for identifying ACM with the lowest false positive prediction in non-ACM samples. The acquired hyperspectral data were first examined using principal component analysis. Then three classification models were built, and the results were compared in order to find the most robust and reliable strategy for recognizing C&DW and identifying ACM and asbestos fibers. In particular, a hierarchical partial least squares-discriminant analysis (Hi-PLSDA), a principal component analysis k-nearest-neighbors (PCA-kNN), and in the end, Error Correcting Output Codes Support Vector Machine (ECOC-SVM) were applied. Their performances were evaluated in terms of prediction maps

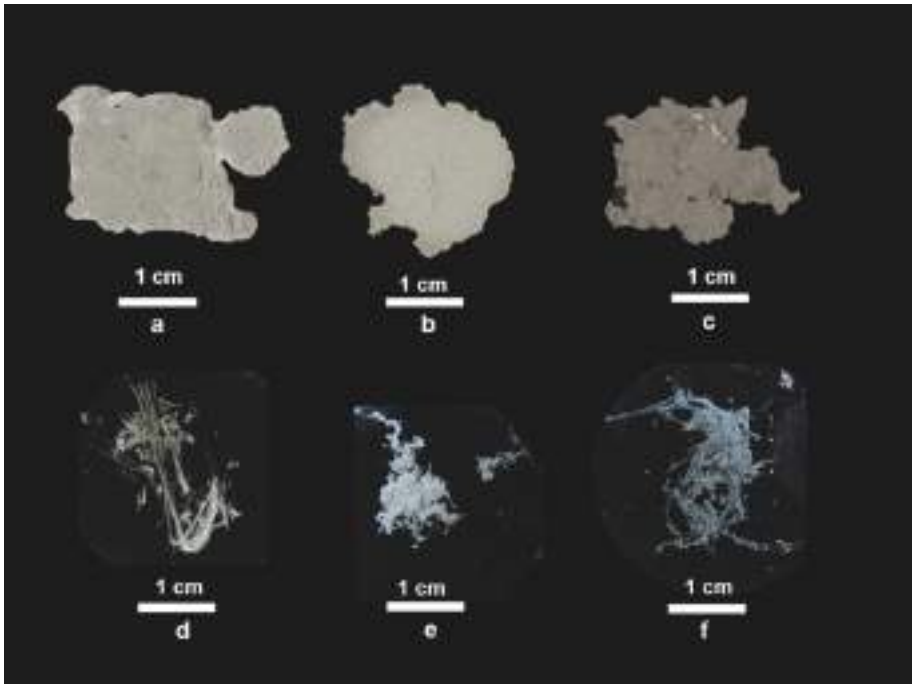

Fig. 1. RGB colour images of the acquired milled and raw fibrous asbestos samples used for calibration dataset, composed of: (a) milled amosite sample, (b) milled chrysotile sample, (c) milled crocidolite sample, (d) raw amosite sample, (e) raw chrysotile sample and (f) raw crocidolite sample.

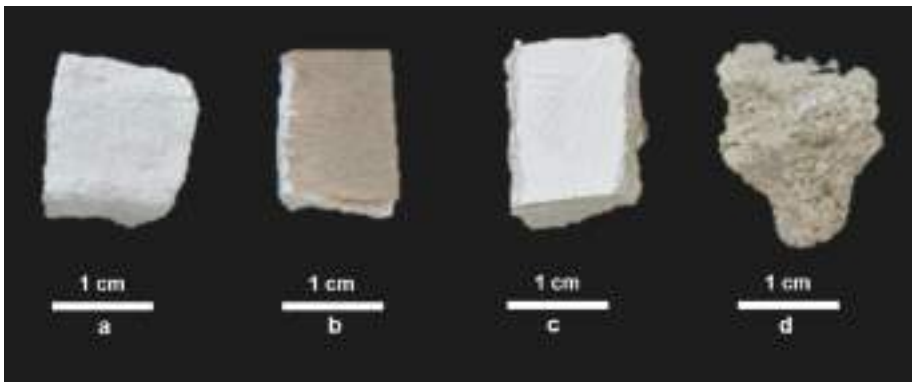

Fig. 2. RGB colour images of the acquired C&DW samples used for calibration dataset, composed of: (a) Plasterboard (inside) sample, (b) Plasterboard (back side) sample, (c) Plasterboard (front side, covered by Plaster) sample and(d) Concrete sample.

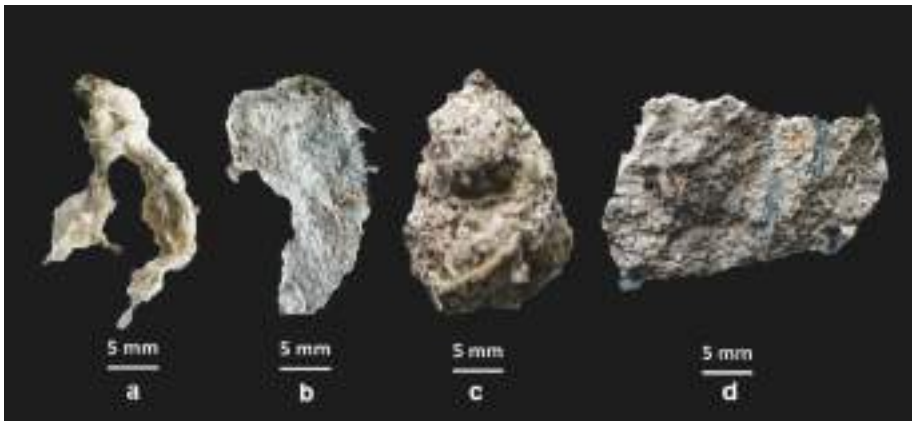

Fig. 3. RGB colour images of the acquired ACM samples used for calibration dataset, composed of: (a) chrysotile rope, (b) chrysotile and crocidolite in a cement matrix, (c) amosite in a cement matrix and (d) chrysotile and crocidolite in a cement matrix.

and statistical parameters. Moreover, micro-X-ray fluorescence (micro-XRF) maps were obtained and compared with the HSI prediction maps.

2. Materials and methods

The investigated samples

For this study, different samples were investigated in order to create a calibration and validation dataset, that is:

- Asbestos (raw and milled) and Asbestos Containing Material (ACM) samples were provided and certified by the National Institute for Insurance against Accidents at Work (INAIL) and characterized in previous work [20]. In particular, these samples containing amosite $(Fe^{2+})_2(Fe^{2+}, Mg)_5Si_8O_{22}(OH)_2$), chrysotile $Mg_3(Si_2O_5)$ $(OH)_4$ and crocidolite $Na_2(Mg, Fe)_6Si_8O_{22}(OH)_2$ fibers.
- C&DW samples were provided by COSMARI, a stationary recycling plant located in Macerata (Italy) province, responsible for sorting and managing post-earthquake debris. Among these samples, concrete and plasterboard were selected as they are among the most used in the construction sector. In particular, concrete and cement matrices are the most used in combination with asbestos fibers to obtain ACM. Moreover, plaster was also included in the dataset inasmuch was present on the top of the plasterboard.

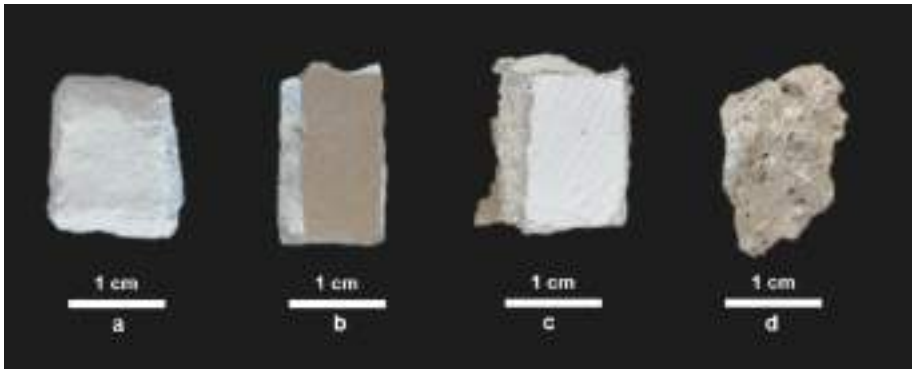

Fig. 4. RGB colour images of the acquired C&DW samples used for validation dataset, composed of: (a) Plasterboard (inside) sample, (b) Plasterboard (back side) sample, (c) Plasterboard (front side, covered by Plaster) sample and (d) Concrete sample.

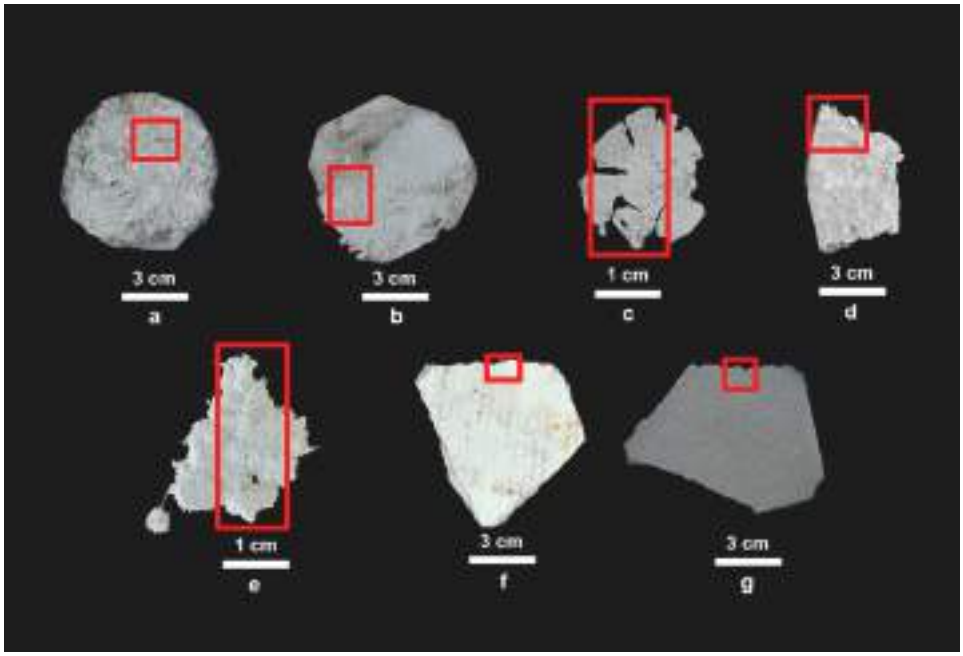

Fig. 5. RGB colour images of the acquired ACM samples used for validation dataset, composed of: (a) amosite insulator product, (b) chrysotile rope, (c) chrysotile mortar, (d) chrysotile gasket, (e) milled chrysotile fibers, (e) insulator product, (f) asbestos panel and (g) asbestos panel. In the red box the samples used in the validation dataset are highlighted. (For interpretation of the references to colour in this figure legend, the reader is referred to the web version of this article.)

More in detail, the calibration dataset was built with three milled and three raw asbestos samples (Fig. 1), four C&DW samples (Fig. 2) and four different typologies of ACM (Fig. 3).

In order to test and compare the classification model results, a validation dataset was created by four C&DW samples (concrete and plasterboard) (Fig. 4) and seven ACM samples (Fig. 5): amosite insulator product, chrysotile rope, chrysotile mortar, chrysotile gasket, milled chrysotile fibers, insulator product, asbestos panel, asbestos panel. The different ACM samples have been identified and characterized following a micro-X-ray Fluorescence approach, and the results have been compared with those of prediction maps.

In total, six classes of samples were investigated: concrete, plaster, plasterboard, amosite, crocidolite and chrysotile.

Hyperspectral imaging system

Hyperspectral imaging acquisitions were carried out at RawMaLab of the Department of Chemical Engineering, Materials and Environment (Sapienza - University of Rome, Italy). Hyperspectral images were acquired using SISUChema XL™ Chemical Workstation (Specim, Finland) equipped with ImSpector™ N25E imaging spectrograph (Specim, Finland) working in the SWIR range (1000–2500 nm). A macro lens with a field of view of 10 mm was adopted, with a resolution of 30 μm/pixel, allowing to perform asbestos identification of classification. ChemaDAQ™ software was used to acquire and collect hyperspectral data.

Data processing and image analysis

Hyperspectral data pre-processing

Hyperspectral data were analyzed utilizing the PLS_Toolbox (Eigenvector Research, Inc.) running inside MATLAB (The Mathworks, Inc., Natick, MA, USA) to perform PCA and Hi-PLSDA, and Statistics and Machine Learning Toolbox™ for Principal Component Analysis k-Nearest Neighbors (PCA-kNN) and Error Correcting Output Coding with Support Vector Machines (ECOC-SVM) classification models.

Spectral data were pre-processed using a combination of algorithms to highlight the differences between the classes and optimize the recognition. In the following a brief description of the adopted pre-processing procedures is reported:

- Multiplicative Scatter Correction (MSC) is one of the most used algorithms that reduce the scattering effects [21].
- Standard Normal Variate (SNV) allows the resolution of source or detector variations or other general instrumental sensitivity effects. It is one of the most used algorithms for correcting scattering effects [22].
- Derivative is an algorithm for removing baseline signal from samples, where each variable in a sample is subtracted from its immediate neighboring variable [21].
- Mean Center (MC) is a method for deleting data offsets that are not of interest for the interpretation of data variance and is a type of Centering algorithm that corresponds to a translation of the axis origin at the centroid of the data [23].

Principal Component Analysis (PCA)

After pre-processing, an exploratory analysis was performed by applying PCA to the spectral data [24]. PCA is an unsupervised method that reduces the data dimensionality by projecting samples into a lower-dimensional subspace, where the axes (i.e., principal components - PC) point in the direction of maximum variance. The first few PCs, resulting from PCA, are generally used to analyze the standard features among samples and their grouping: in fact, samples characterized by similar spectral signatures tend to aggregate in the score plots of the first two or three components. PCA was thus utilized to remove the background and evaluate the best pre-processing combinations according to the separation in the score plots of the six classes [24,25]. In order to process and build PCA-kNN and ECOC-SVM models, data reduction was made using PCA.

Classification models and performance metrics

In order to define the best model able to identify ACM and C&DW, three models were created and tested. More in detail, a hierarchical approach based on PLS-DA was selected as the most common classification model based on the covariance or variance of the data [26]. A PCA-kNN was then adopted, it is a 'mixed' classification method combining a linear approach with a nonlinear one [27]. Finally, an ECOC-SVM was also applied: it represents an effective strategy for solving multiple classification tasks by splitting them into many two-

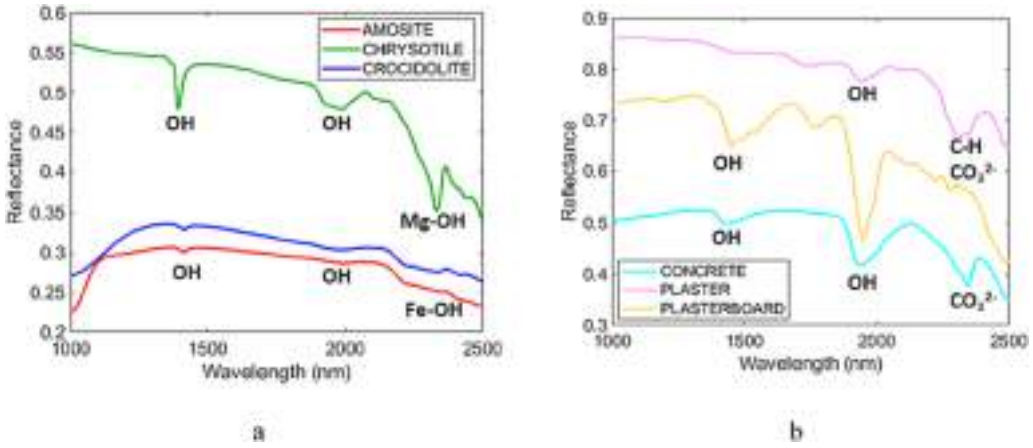

Fig. 6. Average raw reflectance spectra of: (a) amosite, chrysotile and crocidolite classes and (b) concrete, plaster, plasterboard classes.

classification ones [28].

The calibration dataset was used to train the different models, in which each pixel is assigned to a class. Then a cross-validation phase is performed in order to define the principal components/latent variables and choose the correct complexity of the model. In the end, each model was tested on the validation dataset, and the metric performances of *Sensitivity* and *Specificity* were evaluated.

Moreover, the prediction results obtained by the three-classification models were compared with the micro-XRF maps obtained for each sample in order to validate the model.

A detailed description of each classifier is reported in the following.

Hierarchical Partial Least Squares - Discriminant Analysis (Hi-PLSDA)

PLS-DA is a supervised technique allowing to build a model that predicts known classes in an unknown image. It is a classification technique combining the partial least squares regression features with the discriminant ability of a classification technique. In PLS-DA a prior knowledge of the data is required, indeed known samples were used to build the model able to predict unknown ones [26,29,30]. In this work, a hierarchical PLS-DA was developed, where each object is divided according to its differences and isolated from each other into subsets and then into further subsets until each subset contains a single object. For each object, a PLS-DA classification model was performed. An example of the Hi-PLSDA result is shown in Fig. S1 through a dendrogram.

PCA-kNN

PCA-kNN classification is one of the most basic and simple algorithms used in classification methods. It is a powerful non-parametric classification system based on no prior knowledge of the data distribution [31]. kNN classification was developed to perform discriminant analysis when reliable parametric estimates of probability densities are unknown or difficult to obtain [31]. The kNN classification algorithm attempts to find the k nearest neighbors of a query vector and uses a majority vote to determine its class label among the predefined classes. Without prior knowledge, the kNN classifier usually uses Euclidean distance as a distance metric. The performance of a kNN classifier is primarily determined by the choice of k and the distance metric applied [32].

ECOC-SVM

The Support Vector Machine (SVM) approach is a powerful tool based on a classical machine learning method used in data science and chemometric analysis for classification [33] and regression of complex systems [34]. SVM is a reliable and efficient method for spectral data. It is based on a supervised classification method with good generalization capabilities that can efficiently handle linear and nonlinear data [35–37]. This approach optimizes a trade-off between the training instances' accuracy and the function's complexity and is usually defined for binary classification tasks. Instead, the ECOC framework was suitable for solving multiclass learning problems [28].

Classification performance metrics

The parametric performances of the three selected classification methods were evaluated and compared in terms of the values assumed by the statistical parameters: Sensitivity and Specificity in calibration ad cross-validation [38]. Sensitivity expresses the ability of the model to detect samples belonging to the class in question correctly and is defined by equation (2), in which TP represents the total number of true positives and FN the total number of false negatives. Sensitivity expresses the model ability to recognize samples belonging to the considered class correctly, and it is defined by Equation (1), in which TP represents the total number of True Positive and FN the total number of False Negative. Specificity describes the model ability to reject samples belonging to all the other classes correctly and it is defined by Equation (2), in which TN represents the total number of True Negative and FP the total number of False Positive. *Sensitivity and Specificity* can assume values between 0 and 1, the latter being the ideal value for a prediction model.

$$Sensitivity : TP/(TP + FN) \quad (1)$$

$$Specificity : TN/(TN + FP) \quad (2)$$

Micro X-ray fluorescence

Micro-XRF analyses were carried out at the RawMaLab (Raw Materials Laboratory) of the Department of Chemical Engineering, Materials & Environment (Sapienza - University of Rome, Italy) using a Bruker Tornado M4 equipped with an Rh tube, operating at 50 kV, 200 μA, with a 25 μm spot obtained with poly-capillary optics. Mapping acquisition conditions are 10 ms/pixel and step size 100 μm in vacuum at 25 mBar.

The analyzed elements for the identification of asbestos material are silicon (Si), magnesium (Mg) and iron (Fe). More in detail, amosite and crocidolite were recognized by the presence of Fe. Instead, the Chrysotile was recognized by the presence of Mg. The mosaics of two-element maps, particularly the combination of Si-Mg and Si-Fe, were compared with those obtained by HSI classification.

3. Experimental results

Raw and pre-processed average reflectance spectra

The raw and pre-processed average reflectance spectra of the six classes of the selected samples are reported in Fig. 6, for asbestos (Fig. 6a) and C&DW samples (Fig. 6b), respectively. Amosite spectra was mainly characterized by absorption around 1380 and 1420 nm, related to the OH group of 1st overtone [39]; absorptions from 2313 to 2353 nm show characteristic frequencies related to Fe-OH stretching vibrations [39–42]; moreover, an absorption between 1000 and 1050 nm represents Fe^{3+} influence [39,42] (Fig. 6a). Chrysotile shows two strong and characteristic absorptions at 1370–1450 nm and 1909 nm due to the

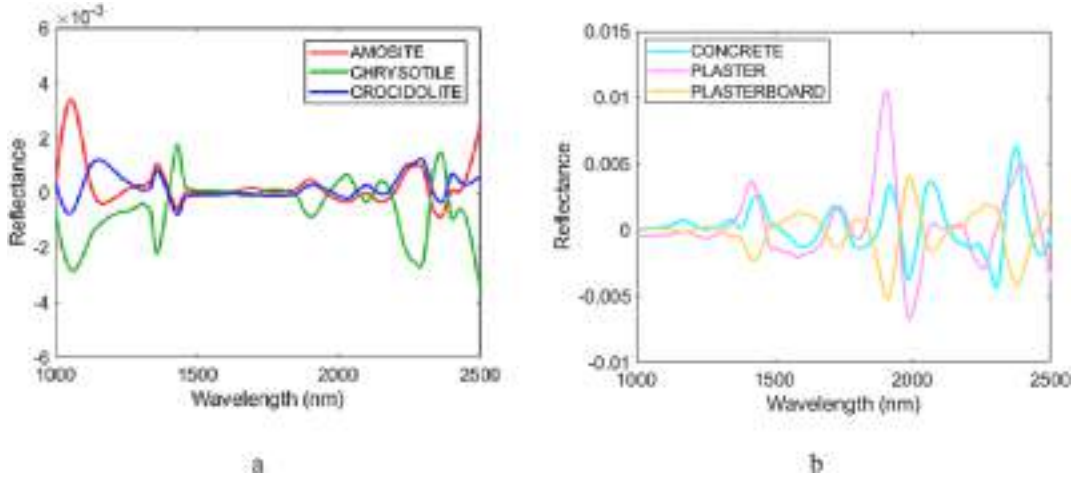

Fig. 7. Pre-processed reflectance spectra of: (a) amosite, chrysotile and crocidolite classes and (b) concrete, plaster, plasterboard classes.

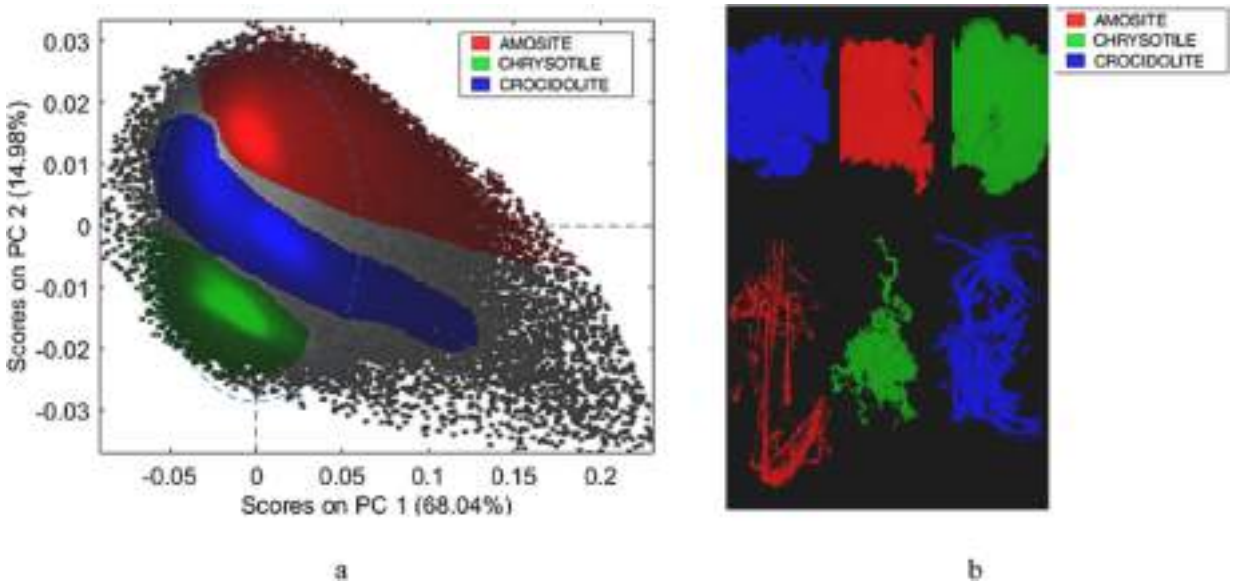

Fig. 8. (a) PCA score plot of amosite, chrysotile and crocidolite classes, and (b) image of score representative of the classes set on the PCA score plot.

hydroxyl group of the 2nd overtone region [40,41]; furthermore, a significant absorption feature is located from 2308 to 2388 nm, attributed to the hydroxyl combination band of Mg-OH [40–43] (Fig. 6a). Crocidolite shows absorptions around 1050 nm due to iron influence [39,42] and around 1420 nm, related to the hydroxyl group of the combination band [40,41]; moreover, absorption features of amphiboles occur in the 2320 nm and 2380 nm wavelength regions [39–42], overlapping with di- and tri-octahedral phyllosilicates containing Fe^{3+} [39,42] (Fig. 6a).

Concrete class is characterized by absorptions around 1454 and 1921 nm due to overtones caused by OH and molecular water, respectively [39]; the absorption at 2330–2380 nm is related to CO_3^{2-} [44–46] (Fig. 6b). Plasterboard spectra present absorption features around 1454, 1750, 1950 and 2221 nm. Bands located near 1450 and 1950 nm are produced by OH stretching [39]; most of the features displayed can be explained in terms of overtone and combination tones of the molecular water, which are essential in the gypsum structure [47–49] (Fig. 6b). Plaster expresses absorption at 1905 nm, due to the hydroxyl group (OH^-) of the 2nd overtone region, absorption at 2000 nm attributed to OH^- of the 1st overtone region [39] and, two absorptions around 2300 nm and 2310 nm mainly related to C–H bond and CO_3^{2-} [39,44,50] (Fig. 6b).

In order to emphasize the spectral features identified in the six classes, data were sequentially pre-processed with the following algorithms: MSC, Derivative and MC (Fig. 7).

PCA results

The PCA score plot related to raw and milled asbestos samples show three different clouds, representative of the selected asbestos reference samples (Fig. 8). The PC1-PC2 scores highlight 3 different clusters corresponding to the 3 types of analyzed asbestos (i.e., amosite, chrysotile and crocidolite). The PCA model confirms that the preprocessing strategy allows to identify the three asbestos minerals independently from their texture (i.e., fibrous or milled material).

To evaluate the spectral feature and the variability of asbestos fibers compared to C&DW samples, three PCA were investigated and reported in the following (Fig. 9). The analyzed PCA score plots show a complex scenario with clusters of asbestos fibers close to those of the different C&DW materials.

In detail, the PCA score plot in Fig. 9a shows the variability related to asbestos fibers and concrete. The score plot of PC1 and PC2 shows four main clouds representing the selected asbestos references and concrete samples. Concrete and chrysotile classes are mainly concentrated in the

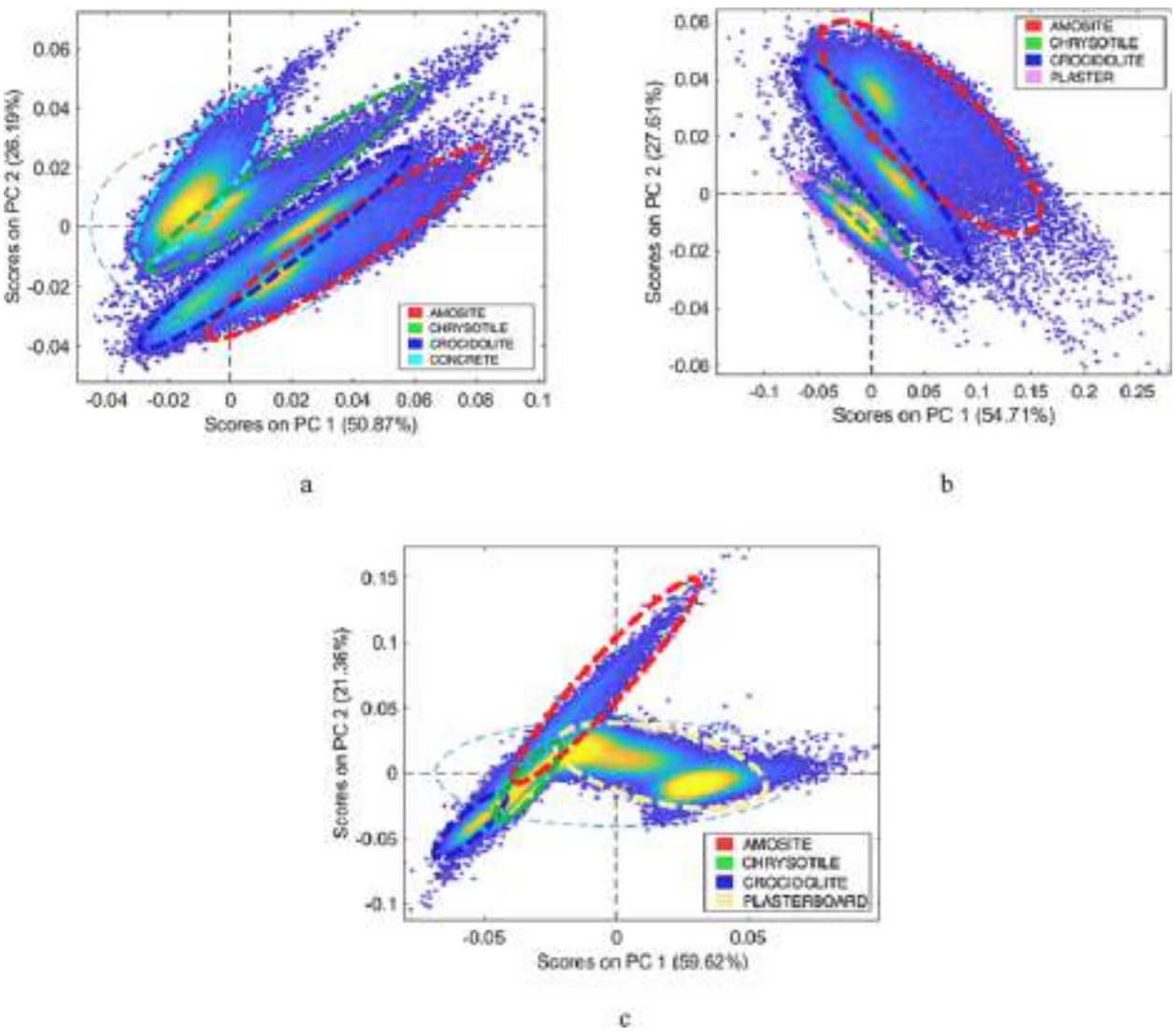

Fig. 9. PCA score plots of: (a) PC1-PC2 representative of amosite, chrysotile, crocidolite and concrete classes, (b) PC1-PC2 representative of amosite, chrysotile, crocidolite and plaster classes and (c) PC1-PC2 representative of amosite, chrysotile, crocidolite and plasterboard classes.

second quadrant, close to each other and almost intersecting, whereas amosite and crocidolite clusters show very close clouds.

The PCA score plot in Fig. 9b shows the variability related to asbestos fibers and plaster. The PC1-PC2 score shows two clouds in the first and second quadrants, close to each other, belonging to amosite and crocidolite classes. Plaster and chrysotile classes are mainly concentrated in the third quadrant, which are not well separated and almost overlapping.

Finally, in Fig. 9c, the PCA score plot shows the variability related to asbestos fibers and plasterboard. In the PC1-PC2 score plot, the plasterboard cloud almost intersects with the amosite and chrysotile clusters, showing a larger variability. Moreover, the chrysotile and crocidolite clusters are mainly concentrated in the third quadrant, almost overlapped and not well separated.

Starting from the results obtained through the PCA models, in order to improve the spectral variability and create a more representative calibration model, four samples of ACM, in which the fibers have been previously characterized [20], were added.

Classification model results

Hi-PLSDA

Starting from the calibration dataset, a hierarchical PLS-DA model based on 9 rules was defined, set up and cross-validated, adopting a Venetian blind with window data splits equal to 10 and 1 sample per spectrum for each rule (Fig. 10).

Rule 1 has been adopted to remove the background.

Rule 2 allowed to perform the further four steps of classification to be carried out, enabling the identification in the next three rules (Rule 3–4-5) of C&DW materials (concrete, gypsum and gypsum board) from the raw asbestos minerals. A further "refinement" (Rule 6) allowed the identification of different types of raw asbestos (amosite, chrysotile and crocidolite).

More in detail, Rule 3 classifies chrysotile from the macro-class amosite/crocidolite/concrete. Rule 4 recognizes chrysotile and plaster from the macro-class amosite/crocidolite. Rule 5 separates chrysotile and plasterboard from the macro-class amosite/ crocidolite. Rule 6 identifies the raw fibers of amosite, chrysotile and crocidolite. Rule 7 separates concrete from crocidolite and amosite in ACM samples. Rule 8 and Rule 9 classify amosite from crocidolite from the output of plaster and plasterboard, respectively (Rule 4 and Rule 5).

Different pre-processing algorithms sequence was adopted for each rule to perform the separation between classes. The pre-processing strategy selected for each rule are summarized in Table 1.

The correctness of the developed Hi-PLSDA, for each rule, was evaluated by Sensitivity and Specificity in Calibration (Cal) and Cross-Validation (CV), as reported in Table 2. It can be noticed as the Hi-PLSDA classifiers show high-quality parametric performances. In

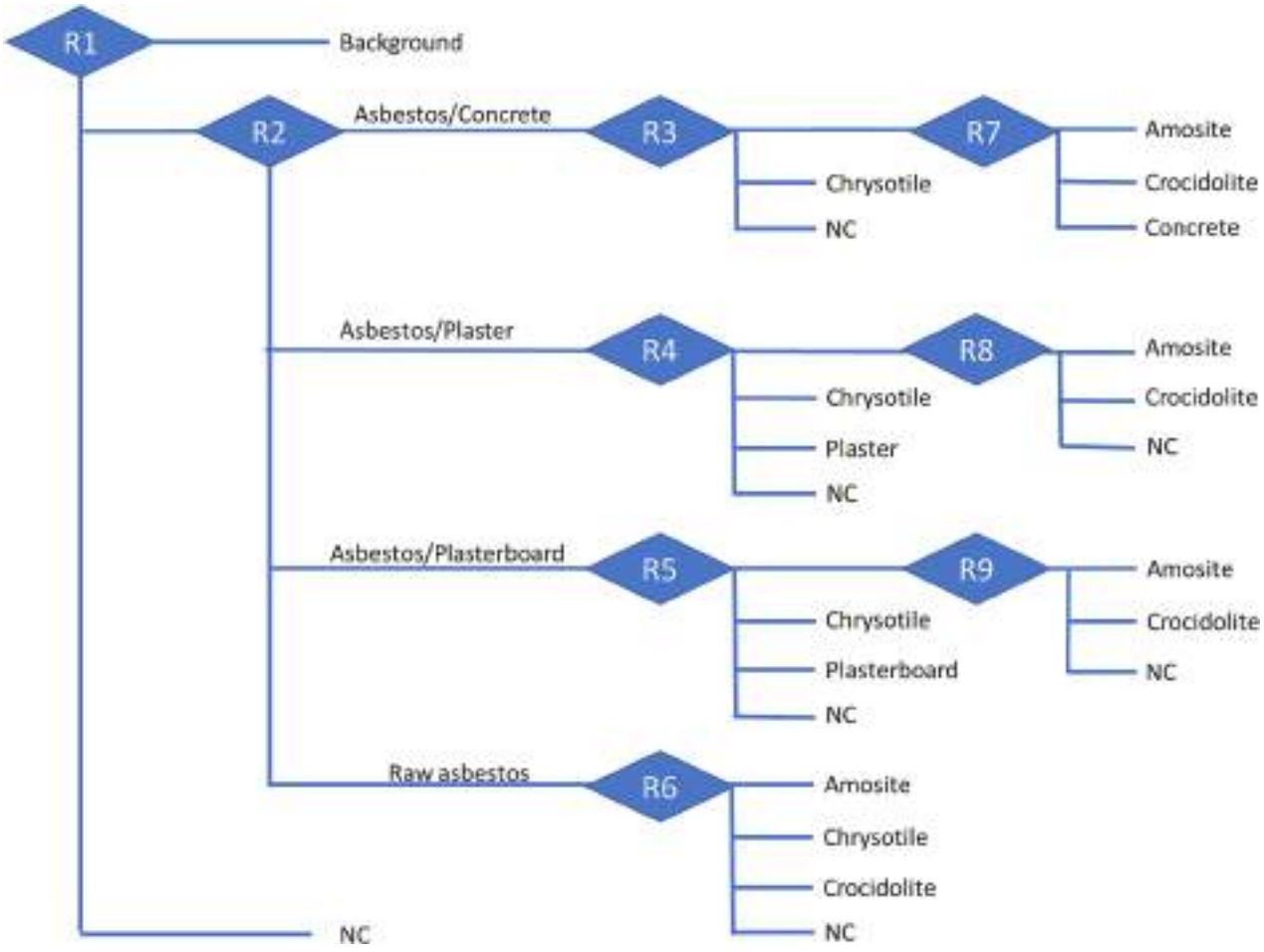

Fig. 10. Dendrogram showing the hierarchical model built to classify the ACM and C&DW classes.

Table 1
Description of the pre-processing strategies sequences applied to the spectra for each rule of Hi-PLSDA model.

Rule	Pre-processing
1	Multiplicative Scatter Correction (MSC) (median) 1st Derivative (window: 15) Mean Center
2	Multiplicative Scatter Correction (MSC) (median) Mean Center
3	Multiplicative Scatter Correction (MSC) (median) 1st Derivative (window: 11) Mean Center
4	Multiplicative Scatter Correction (MSC) (median) 1st Derivative (window: 27) Mean Center
5	Multiplicative Scatter Correction (MSC) (median) 1st Derivative (window: 11) Mean Center
6	Multiplicative Scatter Correction (MSC) (median) 1st Derivative (window: 21) Mean Center
7	Standard Normal Variate (SNV) 1st Derivative (window: 15) Mean Center
8	Multiplicative Scatter Correction (MSC) (median) 1st Derivative (window: 11) Mean Center
9	Multiplicative Scatter Correction (MSC) (median) 1st Derivative (window: 15) Mean Center

detail, Sensitivity ranges from 0.89 to 1.00 in Calibration and from 0.89 to 1.00 in CV, and *Specificity* values range from 0.92 to 1.00 in Calibration and from 092 to 1.00 in Cross-Validation.

PCA-kNN results

PCA-kNN model was evaluated in terms of Sensitivity and Specificity (Table 3). In detail, Sensitivity ranging 0.94 (i.e., crocidolite class) to 1.00 (i.e., plaster and plasterboard classes), and Specificity ranges from 0.99 (i.e., chrysotile class) to 1.00 (i.e., plaster and plasterboard classes), both in Calibration and Cross-Validation. The results in terms of parametric performance (Table 3) confirm the excellent quality of the model.

ECOC-SVM results

The classification results obtained by ECOC-SVM in terms of Sensitivity and Specificity in Calibration and Cross-Validation (Table 4) are similar to those obtained by the PCA-kNN model, with slightly low values in both the parameters. In more detail, Sensitivity ranges from 0.88 (i.e., crocidolite class) to 1.00 (i.e., plaster and plasterboard classes), and Specificity ranges from 0.98 (i.e., concrete class) to 1.00 (i.e., plaster and plasterboard classes), both in Calibration and Cross-Validation (Table 4).

Classification results in prediction

The three developed classification models were tested on different samples to evaluate their performance in prediction. More in detail, the models were carried out on C&DW samples in order to evaluate the false positive recognition of asbestos fibers, and thereafter, the models were tested on ACM samples. In order to verify the accuracy of the models, the prediction results were compared with those obtained by micro-XRF maps.

Results of C&DW samples

The prediction maps obtained from the three models applied to

Table 2
Sensitivity and *Specificity* in calibration (Cal) and cross-validation (CV) for each rule of Hi-PLSDA model.

R1		All classes	Background	
	Sensitivity (Cal)	0.95	0.99	
	Specificity (Cal)	0.99	0.95	
	Sensitivity (CV)	0.95	0.99	
	Specificity (CV)	0.99	0.95	
R2		Concrete	Plaster	Plasterboard
	Sensitivity (Cal)	1.00	1.00	1.00
	Specificity (Cal)	0.99	1.00	1.00
	Sensitivity (CV)	0.96	1.00	1.00
	Specificity (CV)	1.00	0.95	1.00
R3		Amosite-Crocidolite-Concrete	Chrysoltile	
	Sensitivity (Cal)	0.98	0.92	
	Specificity (Cal)	0.92	0.98	
	Sensitivity (CV)	0.99	0.95	
	Specificity (CV)	0.95	0.99	
R4		Amosite-Crocidolite	Chrysoltile	Plaster
	Sensitivity (Cal)	0.98	0.90	1.00
	Specificity (Cal)	0.93	0.93	0.99
	Sensitivity (CV)	0.99	0.93	1.00
	Specificity (CV)	0.95	0.97	1.00
R5		Chrysotile	Plasterboard	Amosite-Crocidolite
	Sensitivity (Cal)	0.89	1.00	0.95
	Specificity (Cal)	0.98	0.98	0.94
	Sensitivity (CV)	0.89	1.00	0.95
	Specificity (CV)	0.98	0.98	0.94
R6		Amosite	Chrysoltile	Crocidolite
	Sensitivity (Cal)	0.92	0.89	0.93
	Specificity (Cal)	0.98	0.93	0.94
	Sensitivity (CV)	0.96	0.90	0.92
	Specificity (CV)	0.97	0.98	0.94
R7		Amosite	Crocidolite	Concrete
	Sensitivity (Cal)	0.98	0.93	0.92
	Specificity (Cal)	0.98	0.94	0.92
	Sensitivity (CV)	0.98	0.93	0.92
	Specificity (CV)	0.98	0.94	0.92
R8		Amosite	Crocidolite	
	Sensitivity (Cal)	0.99	0.97	
	Specificity (Cal)	0.97	0.99	
	Sensitivity (CV)	0.99	0.97	
	Specificity (CV)	0.97	0.99	
R9		Amosite	Crocidolite	
	Sensitivity (Cal)	0.99	0.97	
	Specificity (Cal)	0.97	0.99	
	Sensitivity (CV)	0.99	0.97	
	Specificity (CV)	0.99	0.97	

C&DW samples are reported in Fig. 11. Comparing the prediction maps with the corresponding RGB colour image, it is possible to observe a good recognition of plasterboard, plaster and concrete samples.

Few misclassifications occur due to the morphology of the samples, showing that some regions are not perfectly in focus, thus affecting pixels quantification. More in detail, each sample obtained by the three prediction maps was quantitatively evaluated by the population statistics. The results show that some asbestos classes (amosite, chrysotile and crocidolite classes) pixels were incorrectly assigned to C&DW samples. In particular, the Hi-PLSDA model wrongly assigned 67 pixels to the amosite class, 414 pixels to the chrysotile class and 319 pixels to the crocidolite class. On the contrary, the PCA-kNN model wrongly assigned 5789 pixels to the amosite class, 931 pixels to the chrysotile class and 5 to the crocidolite class. Finally, the ECOC-SVM model incorrectly assigns 1489 pixels to the amosite class and 591 pixels to the chrysotile class.

The Hi-PLSDA model shows the best performance in terms of true negative detection with few misclassified pixels in asbestos classes, followed by ECOC-SVM and PCA-kNN. The highest number of misclassification pixels, for both ECOC-SVM and PCA-kNN results, were detected in the edges of concrete and plasterboard samples. The detected classification errors are mainly due to the high variability of concrete materials and the edge effect of the analysed samples.

Results of ACM samples

Amosite insulator product

The insulator product sample was identified and classified as amosite by all the three HSI-based models and the micro-XRF map confirmed such result (Fig. 12). More in detail, the presence of iron (Fe) and silicon (Si) in Fig. 12e can be associated to the distribution of amosite fibers, covering all the acquired area.

The classification results obtained by Hi-PLSDA, PCA-KNN and ECOC-SVM show similar results in recognition of amosite inside the insulator product.

Chrysotile rope

The prediction maps for the chrysotile rope sample obtained by the application of the three different HSI-based models provided different results (Fig. 13). In particular, the Hi-PLSDA prediction map (Fig. 13a) shows the presence of chrysotile on the entire investigated area, whereas in PCA-kNN and ECOC-SVM prediction maps (Fig. 13b and 13c, respectively), it was detected a variable amount of concrete with chrysotile, greater in the latter case. The correctness of classification results, especially for the first two models, are confirmed by the micro-XRF map obtained on the same sample area, allowing to identify the distribution of chrysotile based on the presence of magnesium (Mg) (Fig. 13d).

Table 3
Sensitivity and Specificity in calibration (Cal) and cross-validation (CV) for PCA-kNN model.

	Class	Amosite	Chrysotile	Crocidolite	Concrete	Plaster	Plasterboard
PCA-kNN	*Sensitivity* (Cal)	0.99	0.99	0.94	0.94	1.00	1.00
	Specificity (Cal)	0.99	1.00	0.99	0.99	1.00	1.00
	Sensitivity (CV)	0.99	0.99	0.94	0.94	1.00	1.00
	Specificity (CV)	0.99	1.00	0.99	0.99	1.00	1.00

Table 4
Sensitivity and *Specificity* in calibration (Cal) and cross-validation (CV) for ECOC-SVM model.

	Class	Amosite	Chrysotile	Crocidolite	Concrete	Plaster	Plasterboard
ECOC-SVM	*Sensitivity* (Cal)	0.95	0.95	0.88	0.92	1.00	1.00
	Specificity (Cal)	0.99	0.99	0.98	0.98	1.00	1.00
	Sensitivity (CV)	0.95	0.95	0.88	0.92	1.00	1.00
	Specificity (CV)	0.99	0.99	0.98	0.98	1.00	1.00

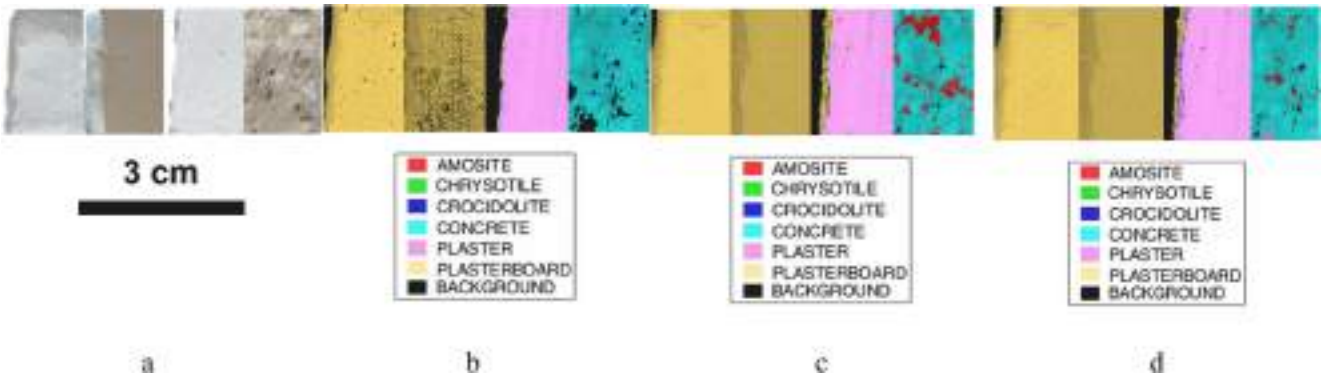

Fig. 11. (a) RGB colour image of the acquired C&DW samples (plasterboard, plaster and concrete) and prediction maps of the three developed HSI-based classification models: (b) Hi-PLSDA, (c) PCA-kNN and (d) ECOC-SVM.

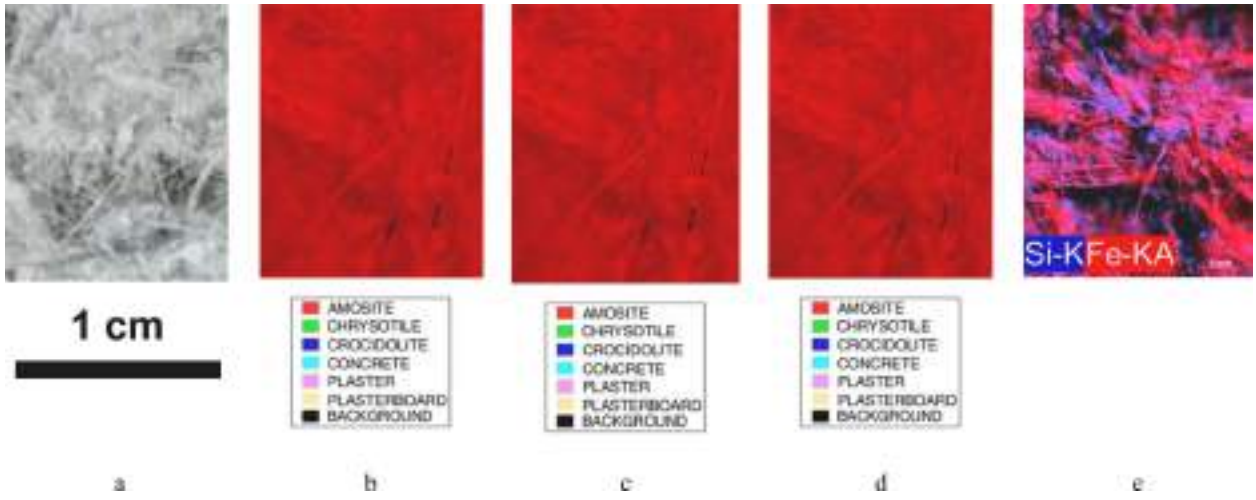

Fig. 12. (a) RGB colour image detail of the acquired amosite insulator product sample and prediction maps of the three developed HSI-based classification models: (b) Hi-PLSDA, (c) PCA-kNN, (d) ECOC-SVM, and (e) micro-XRF map of the same sample showing the main detected elements (Fe and Si).

Chrysotile mortar

The prediction maps obtained by the application of the three developed HSI-based classification models are shown in Fig. S2. The sample was classified as chrysotile by the three models, with some misclassified pixels attributed to crocidolite in the case of ECOC-SVM map (Fig. S2d). The correctness of classification results, especially for the first two models, are confirmed by the micro-XRF map obtained on the same sample area, allowing to identify the distribution of chrysotile based on the presence of high magnesium (Mg), compared with silicon (Si) (Fig. S2e).

Chrysotile gasket

The prediction maps based on the three HSI classification models for the chrysotile gasket sample are shown in Fig. S3. The sample was classified as chrysotile and three prediction maps showed similar results. The correct identification of chrysotile is confirmed by the micro-XRF map based on the identification of Mg on the entire investigated area

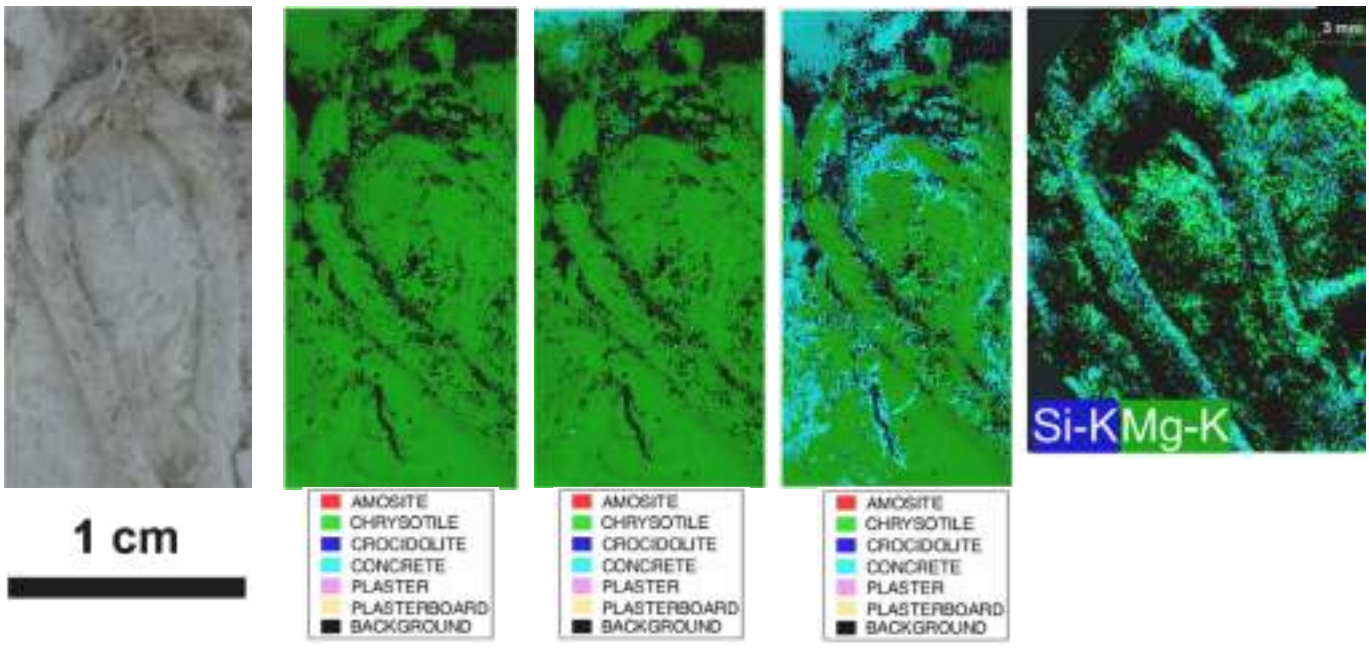

Fig. 13. (a) RGB colour image detail of the acquired chrysotile rope sample and prediction maps of the three developed HSI-based classification models: (b) Hi-PLSDA, (c) PCA-kNN, (d) ECOC-SVM, and (e) micro-XRF map of the same sample showing the main detected elements (Si and Mg).

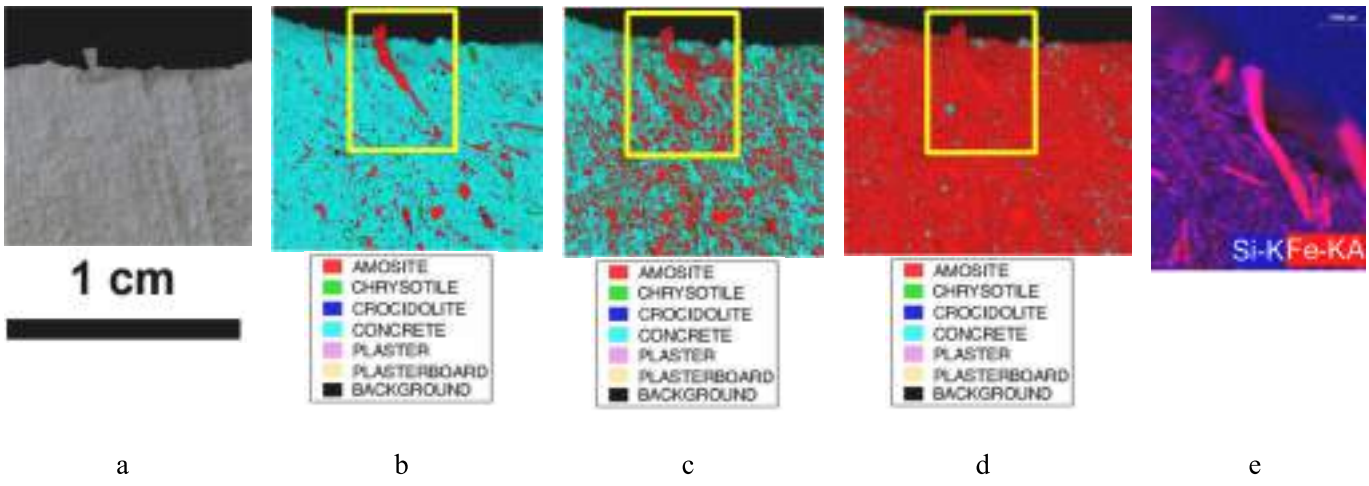

Fig. 14. (a) RGB colour image detail of the acquired asbestos panel sample and prediction maps of the three developed HSI-based classification models: (b) Hi-PLSDA, (c) PCA-kNN, (d) ECOC-SVM, and (e) micro-XRF map of the same sample showing the main detected elements (Si and Fe).Yellow box in the prediction maps correspond to micro-XRF map detail. (For interpretation of the references to colour in this figure legend, the reader is referred to the web version of this article.)

(Fig. S3e).

Chrysotile blending fibers

In Fig. S4 the prediction maps obtained by the application of the three HSI-based classification models to the chrysotile blending fibers sample are shown. The sample was classified as chrysotile by the first two models (Fig. S4b and S4c), whereas in the case of ECOC-SVM model some pixels were incorrectly classified as crocidolite (Fig. S4d). The correctness of classification results, especially for the first two models, are confirmed by the micro-XRF map obtained on the same sample area, allowing to identify the distribution of chrysotile based on the presence of Mg (Fig. S4e).

Asbestos panel 1

In Fig. 14 the prediction maps obtained by the application of the three HSI-based classification models to the asbestos panel 1 sample are shown. The results of Hi-PLSDA prediction maps clearly show how most of the detected fibers were assigned to amosite in the concrete matrix, with few pixels assigned to chrysotile. PCA-kNN model identified more amosite fibers in the concrete matrix compared to those detected by the Hi-PLSDA model. Finally, the ECOC-SVM model assigned almost all the pixels to the amosite class and few pixels to concrete class. Comparing the HSI-based classification results with the micro-XRF map, it can be noticed as Hi-PLSDA results fit better the detected Fe distribution. In fact, the prediction results obtained by PCA-KNN and ECOC-SVM showed an overestimation of amosite in the sample.

Asbestos panel 2

The prediction maps based on the three HSI classification models for the asbestos panel 2 sample are shown in Fig. S5. The Hi-PLSDA prediction map show that the detected fibers were classified as amosite in a concrete matrix, with few fibers assigned to chrysotile.

PCA-kNN results identified more amosite fibers in the concrete matrix compared to those detected by the Hi-PLSDA model, and also a greater number of pixels were attributed to chrysotile, especially at the border of the sample. Finally, ECOC-SVM prediction model assigned almost all the pixels to the amosite class, with some pixels assigned to concrete and to chrysotile.

Comparing the HSI-based classification results with the micro-XRF map related to Fe and Si elements, it appears that Hi-PLSDA model provided the best classification results, even if it does not detect all the asbestos fibers. Furthermore, both PCA-kNN and ECOC-SVM models assigned some pixels to chrysotile class near the border of the sample, furthermore, the latter model overestimated the presence of amosite.

Comparison of the different classification models

The three models in calibration and cross-validation show similar results with slight variations of *Sensitivity* and *Specificity values*. The parametric performances show that, in Cal and CV, the best model is PCA-kNN, followed by Hi-PLSDA and ECOC-SVM.

Instead in prediction, the results referred to C&DW samples highlight how the ECOC-SVM and PCA-kNN models tend to misclassify some pixels by incorrectly assigning them to the asbestos fibers considered. In contrast, Hi-PLSDA shows few misclassified pixels that were not reducing the effectiveness of recognition.

Finally, the three models applied to ACM samples generally show good performances. However, Hi-PLSDA shows a better fit with the results obtained by micro-XRF maps of the same area, while PCA-kNN and ECOC-SVM tend to overestimate the presence of asbestos in the samples. The better performance of the Hi-PLSDA model compared with PCA-kNN and ECOC-SVM is probably due to the possibility of using different pre-processing for each rule in order to maximize the separation and recognition of classes.

4. Conclusions

In the present study, an HSI procedure in the SWIR range was developed and implemented in order to identify and recognize asbestos fibers in construction and demolition materials.

Three different classification models (i.e., Hi-PLSDA, PCA-kNN and ECOC-SVM) were developed and applied to recognize the presence of asbestos, without performing a physical sampling of the material, and to define the most robust strategy for automatic classification.

The results were compared with those obtained by micro-XRF elemental mapping, performed to identify asbestos fibers, and confirm the validity of the proposed HSI-based modelling. The best prediction results were obtained by the Hi-PLSDA model. The main advantage of the Hi-PLSDA (i.e., ensemble methods) was in the use of multiple classification models that perform a better predictive result than the PCA-kNN and ECOC-SVM.

The HSI approach has great potential compared with the traditional analytical protocols currently used on a laboratory scale for asbestos identification. Inasmuch, this system allows rapid identification and less risk of exposure for operators. Moreover, this procedure can be directly applied to unknown materials without physical sampling. For that reason, the proposed SWIR-HSI approach could be profitably implemented in situ to avoid handling hazardous material. Future studies aim to recognize asbestos fibers in different matrices with a high-efficiency degree combining different classification models in an ensemble classification approach.

CRediT authorship contribution statement

G. Bonifazi: Conceptualization, Methodology, Validation, Writing – review & editing. **G. Capobianco:** . **S. Serranti:** Conceptualization, Funding acquisition, Methodology, Project administration, Resources, Supervision, Validation, Writing – review & editing. **O. Trotta:** Data curation, Formal analysis, Investigation, Software, Writing – original draft. **S. Bellagamba:** Conceptualization, Funding acquisition, Investigation, Resources, Writing – review & editing. **S. Malinconico:** Conceptualization, Funding acquisition, Investigation, Resources, Writing – review & editing. **F. Paglietti:** Conceptualization, Funding acquisition, Resources, Writing – review & editing.

Declaration of Competing Interest

The authors declare that they have no known competing financial interests or personal relationships that could have appeared to influence the work reported in this paper.

Data availability

The data that has been used is confidential.

Acknowledgements

The study was developed in the framework of INAIL (Italian National Institute for Insurance against Accidents at Work) project: BRIC ID 60/2 – P9 Asbestos Special Program.

Appendix A. Supplementary material

Supplementary data to this article can be found online at https://doi.org/10.1016/j.saa.2023.123672.

References

[1] EC, 2020. Waste: construction and demolition waste [WWW document]. URL http://ec.europa.eu/environment/waste/construction_demolition.htm (accessed 3.1.20).
[2] J. García-González, D. Rodríguez-Robles, A. Juan-Valdés, J. M. Morán-del Pozo, M. Ignacio Guerra-Romero, Porosity and pore size distribution in recycled concrete. Mag. Concr. Res. 67:22 (2015) 1214-1221. Doi: 10.1680/macr.14.00218.
[3] I. Vegas, K. Broos, P. Nielsen, O. Lambertz, A. Lisbona, Upgrading the quality of mixed recycled aggregates from construction and demolition waste by using near-infrared sorting technology.
[4] Construction and Building Materials, 75, (2015) 121-128. Doi: 10.1016/j.conbuildmat.2014.09.109.
[5] N. Roussat, J. Méhu, M. Abdelghafour, P. Brula, Leaching behaviour of hazardous demolition waste, Waste Manage. 28 (11) (2008) 2032–2040, https://doi.org/10.1016/j.wasman.2007.10.019.
[6] C. Giacobbe, A.F. Gualtieri, S. Quartieri, C. Rinaudo, M. Allegrina, G.B. Andreozzi, Spectroscopic study of the product of thermal transformation of chrysotile-asbestos containing materials (ACM), Eur. J. Mineral. 22 (4) (2010) 535–546, https://doi.org/10.1127/0935-1221/2010/0022-2038.
[7] R.L. Virta, Mineral Commodity Profiles Asbestos U.S. Geology Survey Circular, 1255-KK, Reston. (2005). URL: https://pubsdata.usgs.gov/pubs/circ/2005/1255/kk/index.html.
[8] A.F. Gualtieri, (Eds.), EMU Notes in Mineralogy, Mineral fibres: crystal chemistry, chemical-physical properties, biological interaction and toxicity, 18, (2017) 7-9. ISBN 978-0903056-65-6.
[9] J.E. Craighead, J.L. Abraham, A.A. Churg, F.H. Green, J. Kleinerman, P. Pratt, T.A. Seemayer, V. Vallyathan, H. Weill, The pathology of asbestos-associated diseases of the lungs and pleural cavities: diagnostic criteria and proposed grading schema. Report of the Pneumoconiosis Committee of the College of American Pathologists and the National Institute for Occupational Safety and Health. Archives of pathology & laboratory medicine, 106(11), (1982) 544-596.
[10] Z. Ding, W. Gong, S. Li, Z. Wu, System dynamics versus agent-based modeling: a review of complexity simulation in construction waste management, Sustainability 10 (7) (2018) 2484, https://doi.org/10.3390/su10072484.
[11] M. Rašković, A.M. Ragossnig, K. Kondracki, M. Ragossnig-Angst, Clean construction and demolition waste material cycles through optimised pre-demolition waste audit documentation: a review on building material assessment tools, Waste Manage. Res. 38 (9) (2020) 923–941, https://doi.org/10.1177/0734242X20936763.
[12] H. Jalloul, J. Choi, N. Yesiller, D. Manheim, S. Derrible, A systematic approach to identify, characterize, and prioritize the data needs for quantitative sustainable disaster debris management, Resour. Conserv. Recycl. 180 (2022), 106174, https://doi.org/10.1016/j.resconrec.2022.106174.

[13] L.A.L. Ruiz, X.R. Ramon, S.G. Domingo, The circular economy in the construction and demolition waste sector—a review and an integrative model approach, J. Cleaner Prod. 248 (Mar) (2020), 119238, https://doi.org/10.1016/j.jclepro.2019.119238.
[14] J.D. Linton, J.S. Yeomans, Materials recycling and industrial ecology, Nat. Mater. 3 (4) (2004) 199–201, https://doi.org/10.1038/nmat1101.
[15] A.F. Gualtieri, C. Cavenati, I. Zanatto, M. Meloni, G. Elmi, M. Lassinantti Gualtieri, The transformation sequence of cement-asbestos slates up to 1200 °C and safe re cycling of the reaction product in stoneware tile mixture, J. Hazard. Mater. 152 (2007) 563–570, https://doi.org/10.1016/j.jhazmat.2007.07.037.
[16] S. Serranti, G. Bonifazi, G. Capobianco, S. Malinconico, F. Paglietti, Hyperspectral imaging applied to asbestos containing materials detection: specimen preparation and handling. In Advanced Environmental, Chemical, and Biological Sensing Technologies XV (Vol. 11007, p. 110070S). (2019) International Society for Optics and Photonics. Doi: 10.1117/12.2517070.
[17] G. Bonifazi, G. Capobianco, S. Serranti, Hyperspectral imaging and hierarchical PLS-DA applied to asbestos recognition in construction and demolition waste, Appl. Sci. 9 (21) (2019) 4587, https://doi.org/10.3390/app9214587.
[18] S. Serranti, G. Capobianco, S. Malinconico, G. Bonifazi, Micro X-ray fluorescence imaging coupled with chemometrics to detect and classify asbestos fibers in demolition waste, Detritus 12 (2020) 150–159, https://doi.org/10.31025/2611-4135/2020.14007.
[19] O. Trotta, G. Bonifazi, G. Capobianco, S. Serranti, Detection of asbestos containing material in post-earthquake building waste through Hyperspectral imaging and Micro-X-ray fluorescence, 21, (2022) 27–34. Doi: 10.31025/2611-4135/2022.17233.
[20] G. Bonifazi, G. Capobianco, S. Serranti, Asbestos containing materials detection and classification by the use of hyperspectral imaging, J. Hazard. Mater. 344 (2018) 981–993, https://doi.org/10.1016/j.jhazmat.2017.11.056.
[21] \AA. Rinnan, F. van den Berg, S.B. Engelsen, Review of the most common pre-processing techniques for near-infrared spectra, TrAC Trends Anal. Chem. 28 (2009) 1201–1222, https://doi.org/10.1016/j.trac.2009.07.007.
[22] R.J. Barnes, M.S. Dhanoa, S.J. Lister, Standard normal variate transformation and de-trending of near-infrared diffuse reflectance spectra, Appl. Spectrosc. 43 (1989) 772–777, https://doi.org/10.1366/0003702894202201.
[23] J. Amigo, H. Babamoradi, S. Elcoroaristizabal, Hyperspectral image analysis. A tutorial, Anal. Chim. Acta 896 (2015) 34–51, https://doi.org/10.1016/j.aca.2015.09.030.
[24] S. Wold, K. Esbensen, P. Geladi, Principal component analysis, Chemom. Intell. Lab. Syst. 2 (1987) 37–52, https://doi.org/10.1016/0169-7439(87)80084-9.
[25] R. Bro, A.K. Smilde, Principal component analysis, Anal. Methods 6 (2014) 2812–2831, https://doi.org/10.1039/C3AY41907J.
[26] D. Ballabio, V. Consonni, Classification tools in chemistry. Part 1: Linear models. PLS-DA, Anal. Methods 516 (2013) 3790–3798, https://doi.org/10.1039/C3AY40582F.
[27] G. Serpen, E. Aghaei, Host-based misuse intrusion detection using PCA feature extraction and kNN classification algorithms, Intell. Data Anal. 22 (5) (2018) 1101–1114, https://doi.org/10.3233/IDA-173493.
[28] G. Bakiri, Solving multiclass learning problems via error-correcting output codes, J. Artif. Intell. Res. 2 (1995) 263–286, https://doi.org/10.1613/jair.105.
[29] Y.B. Monakhova, M. Hohmann, N. Christoph, H. Wachter, D.N. Rutledge, Rutledge improved classification of fused data: synergetic effect of partial least squares discriminant analysis (PLS-DA) and common components and specific weights analysis (CCSWA) combination as applied to tomato profiles (NMR, IR and IRMS), Chemom. Intell. Lab. Syst. 156 (2016) 1–6, https://doi.org/10.1016/j.chemolab.2016.05.006.
[30] J.E. Burger, A.A. Gowen, Classification and prediction methods. In: Hyperspectral Imaging Technology in Food and Agriculture; Food Engineering Series; Park, B., Lu, R., Eds.; Springer: New York, NY, USA, 5, (2015) 103–124. 10.1007/978-1-4939-2836-1_5.
[31] H. Parvin, H. Alizadeh, B. Minaei-Bidgoli, MKNN: Modified k-nearest neighbour, in Proceedings of the world congress on engineering and computer science (Vol. 1), (2008, October), Newswood Limited. ISBN: 978-988-98671-0-2.
[32] S.B. Imandoust, M. Bolandraftar, Application of K-nearest neighbor (KNN) approach for predicting economic events: theoretical background, Int. J. Eng. Res. Appl. 3 (2013) 605–610.
[33] Y. Zhang, Q. Cong, Y. Xie, J. Yang, B. Zhao, Quantitative analysis of routine chemical constituents in tobacco by near-infrared spectroscopy and support vector machine, Spectrochim. Acta A Mol. Biomol. Spectrosc. 71 (4) (2008) 1408–1413, https://doi.org/10.1016/j.saa.2008.04.020.
[34] O. Devos, G. Downey, L. Duponchel, Simultaneous data pre-processing and SVM classification model selection based on a parallel genetic algorithm applied to spectroscopic data of olive oils, Food Chem. 148 (2014) 124–130, https://doi.org/10.1016/j.foodchem.2013.10.020.
[35] Y. Langeron, M. Doussot, D.J. Hewson, J. Duchêne, Classifying NIR spectra of textile products with kernel methods, Eng. Appl. Artif. Intel. 20 (3) (2007) 415–427, https://doi.org/10.1016/j.engappai.2006.07.001.
[36] J.A. Fernández Pierna, P. Volery, R. Besson, V. Baeten, P. Dardenne, Classification of modified starches by Fourier transform infrared spectroscopy using support vector machines, J. Agric. Food Chem. 53 (17) (2005) 6581–6585, https://doi.org/10.1021/jf0501544.
[37] T. Zou, Y. Dou, H. Mi, J. Zou, Y. Ren, Support vector regression for determination of component of compound oxytetracycline powder on near-infrared spectroscopy, Anal. Biochem. 355 (1) (2006) 1–7, https://doi.org/10.1016/j.ab.2006.04.025.
[38] D. Ballabio, R. Todeschini, Multivariate classification for qualitative analysis. D.-W. Sun (Ed.), Infrared spectroscopy for quality analysis and control, (2009) 83-104, (N.Y.). ISBN: 978-0-12-374136-3.
[39] Z. Song, C. Kuenzer, Spectral reflectance (400–2500nm) properties of coals, adjacent sediments, metamorphic and pyrometamorphic rocks in coal-fire areas: a case study of Wuda coalfield and its surrounding areas, northern China, Int. J. Coal Geol. 171 (2017) 142–152, https://doi.org/10.1016/j.coal.2017.01.008.
[40] C. Laukamp, K.A. Termin, B. Pejcic, M. Haest, T. Cudahy, Vibrational spectroscopy of calcic amphiboles—applications for exploration and mining, Eur. J. Miner. 24 (2012) 863–878, https://doi.org/10.1127/0935-1221/2012/0024-2218.
[41] C. Laukamp, A. Rodger, M. LeGras, H. Lampinen, I.C. Lau, B. Pejcic, J. Stromberg, N. Francis, E. Ramanaidou, Mineral physicochemistry underlying feature-based extraction of mineral abundance and composition from shortwave, mid and thermal infrared reflectance spectra, Minerals 11 (2021) 347, https://doi.org/10.3390/min1104034722222.
[42] R.N. Clark, T.V.V. King, M. Klejwa, G.A. Swayze, N. Vergo, High spectral resolution reflectance spectroscopy of minerals, J. Geophys. Res. 95 (1990) 12653–12680, https://doi.org/10.1029/JB095iB08p12653.
[43] J.F. Mustard, Chemical analysis of actinolite from reflectance spectra. Am. Mineral., 77, (1992) 345–358. ISSN: 1945-3027.
[44] P.C. Pinet, C. Kaufmann, J. Hill, Imaging spectroscopy of changing Earth's surface: a major step toward the quantitative monitoring of land degradation and desertification, C. R. Geosci. 338 (14–15) (2006) 1042–1048, https://doi.org/10.1016/j.crte.2006.09.012.
[45] J.K. Crowley, D.E. Williams, J.M. Hammarstrom, N. Piatak, I.M. Chou, J.C. Mars, Spectral reflectance properties (0.4–2.5 mm) of secondary Fe-oxide, Fe-hydroxide, and Fe-sulphate-hydrate minerals associated with sulphide-bearing mine wastes, Geochem. Explor. Environ. Anal. 3 (2003) 219–228, https://doi.org/10.1144/1467-7873/03-001.
[46] A.F.H. Goetz, B. Curtiss, D.A. Shiley, Rapid gangue mineral concentration measurement over conveyors by NIR reflectance, spectroscopy, Miner. Eng. 22 (2009) 490–499, https://doi.org/10.1016/j.mineng.2008.12.013.
[47] F.M. Howari, P.C. Goodell, S. Miyamoto, Spectral properties of salt crusts formed on saline soils, J. Environ. Qual 31 (2002) 1453–1461, https://doi.org/10.2134/jeq2002.1453.
[48] J. Farifteh, F. van der Meer, M. van der Meijde, C. Atzberger, Spectral characteristics of salt-affected soils: a laboratory experiment, Geoderma 145 (2008) 196–206, https://doi.org/10.1016/j.geoderma.2008.03.011.
[49] M. Lothodé, V. Carrere, R. Marion, Identifying industrial processes through VNIR-SWIR reflectance spectroscopy of their waste materials, in: 2014 IEEE Geoscience and Remote Sensing Symposium, 2014, pp. 3288–3291, https://doi.org/10.1109/IGARSS.2014.6947182.
[50] S. Cheng, H. Liu, Y. Gao, Preparation and optical properties of waterborne acrylic-based cool white coatings, Chin. Sci. Bull. 59 (31) (2014) 4142–4146, https://doi.org/10.1007/s11434-014-0523-z.